

# FastRSR: Efficient and Accurate Road Surface Reconstruction from Bird’s Eye View

Yuting Zhao\*

Institute of Automation, CAS  
School of Artificial Intelligence, UCAS  
zhaoyuting2023@ia.ac.cn

Xiaoshuai Hao

Beijing Academy of Artificial Intelligence  
xshao@baai.ac.cn

Yuheng Ji\*

Institute of Automation, CAS  
School of Artificial Intelligence, UCAS  
jiyuheng2023@ia.ac.cn

Shuxiao Li†

Institute of Automation, CAS  
shuxiao.li@ia.ac.cn

## ABSTRACT

Road Surface Reconstruction (RSR) is crucial for autonomous driving, enabling the understanding of road surface conditions. Recently, RSR from the Bird’s Eye View (BEV) has gained attention for its potential to enhance performance. However, existing methods for transforming perspective views to BEV face challenges such as information loss and representation sparsity. Moreover, stereo matching in BEV is limited by the need to balance accuracy with inference speed. To address these challenges, we propose two efficient and accurate BEV-based RSR models: *FastRSR-mono* and *FastRSR-stereo*. Specifically, we first introduce Depth-Aware Projection (DAP), an efficient view transformation strategy designed to mitigate information loss and sparsity by querying depth and image features to aggregate BEV data within specific road surface regions using a pre-computed look-up table. To optimize accuracy and speed in stereo matching, we design the Spatial Attention Enhancement (SAE) and Confidence Attention Generation (CAG) modules. SAE adaptively highlights important regions, while CAG focuses on high-confidence predictions and filters out irrelevant information. FastRSR achieves state-of-the-art performance, exceeding monocular competitors by over **6.0%** in elevation absolute error and providing at least a **3.0X** speedup by stereo methods on the RSRD dataset. The source code will be released.

## CCS CONCEPTS

• Computing methodologies → Artificial intelligence.

## KEYWORDS

Autonomous Driving, Road Surface Reconstruction, BEV Perception

\* Equal Contribution.

† Corresponding Author.

Permission to make digital or hard copies of all or part of this work for personal or classroom use is granted without fee provided that copies are not made or distributed for profit or commercial advantage and that copies bear this notice and the full citation on the first page. Copyrights for components of this work owned by others than ACM must be honored. Abstracting with credit is permitted. To copy otherwise, or republish, to post on servers or to redistribute to lists, requires prior specific permission and/or a fee. Request permissions from [permissions@acm.org](mailto:permissions@acm.org).

Conference’17, July 2017, Washington, DC, USA

© 2025 Association for Computing Machinery.

ACM ISBN 978-x-xxxx-xxxx-x/YY/MM...\$15.00

<https://doi.org/10.1145/nnnnnnn.nnnnnnn>

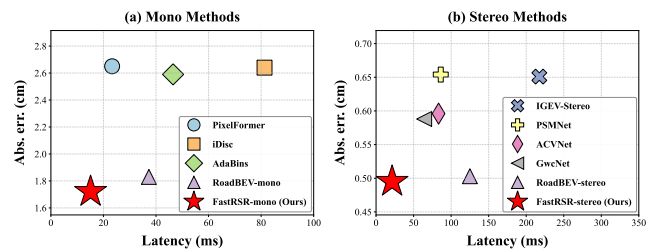


Figure 1: Accuracy vs. Latency on the RSRD [54]. Left: FastRSR-mono outperforms other state-of-the-art monocular depth estimation methods. Right: FastRSR-stereo surpasses published state-of-the-art stereo matching methods.

## 1 INTRODUCTION

Road Surface Reconstruction (RSR) provides valuable and precise information about road surface conditions, which is essential for planning and control in autonomous driving systems [18, 34, 55]. Recently, real-time reconstruction of road surface geometric elevation information has gained increasing attention due to its role in enhancing driving safety and comfort [2, 3, 16]. Therefore, it is crucial to balance the efficiency and accuracy of road surface reconstruction models for practical deployment.

Vision-based Road Surface Reconstruction (RSR) methods offer a cost-effective alternative to LiDAR-based approaches [12, 33, 43, 53], yet they often rely on predicting depth from the Perspective View (PV) before converting it to elevation. This process typically results in sparse informative clues for road surface elevation variation [11, 31, 48]. Recently, RSR from the Bird’s Eye View (BEV) has gained attention for its ability to leverage dense elevation cues and accurately capture profile vibrations [55]. To facilitate the transformation from PV to BEV, existing View Transformation (VT) methods are categorized into three types: 3D-to-2D projection [20, 26, 37, 46], 2D-to-3D projection [19, 22, 24, 25, 35, 56], and fusion projection methods [15, 23, 27]. 3D-to-2D projection methods use 3D voxel coordinates to query images for dense BEV features; however, the lack of depth guidance can lead to indistinguishable voxel features at varying elevations along the same ray, resulting in information loss. On the other hand, 2D-to-3D projection methods project 2D images into 3D space based on depth distribution, but they often suffer from poor elevation information and representation sparsity. Fusion projection methods attempt to combine features from both projection types, facing challenges in

balancing efficiency and accuracy. This paper explores the question: *Can we design an efficient VT strategy specifically tailored for road surface elevation reconstruction?*

In stereo estimation within the Bird's Eye View (BEV) space, we derive the elevation value for a BEV grid by identifying the most similar matching points among elevation candidates from the left and right voxel features along the vertical dimension. This process parallels PV stereo matching [5, 10, 39], where the goal is to find corresponding pixels between image pairs that demonstrate the highest similarity across various disparities. Both approaches fundamentally rely on the same principle: searching for the most similar matching points within a defined search range, allowing us to apply concepts from general stereo matching. However, many existing deep learning-based stereo matching methods typically employ stacked deep 3D convolutional networks to extract effective similarity information from the cost volume, which often results in significant inference time and memory consumption [6, 9, 50]. While there are efficiency-oriented methods that focus on lightweight architectures, these often lead to a considerable degradation in accuracy [40, 44, 51]. Thus, there is a need for a balance between efficiency and accuracy in stereo estimation for BEV applications.

To address these challenges, we propose two efficient and accurate BEV-based RSR models: *FastRSR-mono* and *FastRSR-stereo*. To address information loss and representation sparsity, we introduce the *Depth-aware 3D-to-2D Projection (DAP)* module. This module effectively queries depth and image features to aggregate BEV features using a pre-computed look-up table within designated road surface profile regions. For stereo estimation, to construct informative and compact cost volume representation while mitigating performance degradation in lightweight aggregation networks, we first introduce Spatial Attention Enhancement (SAE) to adaptively select important information from the cost volume, utilizing contextual voxel features. Next, we propose Confidence Attention Generation (CAG) to highlight high-confidence predictions while suppressing irrelevant information with grid-wise confidence weights. Extensive experiments on the real-world RSRD dataset demonstrate the effectiveness of FastRSR, surpassing existing monocular competitors by over 6.0% in elevation absolute error (*Abs. err.*) and achieving at least a 3.0 $\times$  speedup by stereo methods, as shown in Fig. 1.

Our main contributions can be summarized as follows:

- We present two BEV-based RSR models: *FastRSR-mono* and *FastRSR-stereo* for road surface reconstruction, achieving an impressive balance of accuracy and efficiency.
- We propose an effective view transformation strategy named Depth-Aware 3D-to-2D Projection (DAP), which generates dense BEV features with strong representation ability while enjoying cost-effective deployment.
- We introduce the Spatial Attention Enhancement (SAE) module to adaptively enhance important spatial regions from the cost volume. Moreover, we propose a Confidence Attention Generation (CAG) module, which emphasizes high-confidence predictions and suppresses irrelevant information to improve feature representation.
- Our proposed FastRSR achieves superior performance than state-of-the-art (SOTA) methods, which could serve as a strong baseline for road surface reconstruction research.

## 2 RELATED WORK

**Vision-Based Road Surface Reconstruction.** Early research in Road Surface Reconstruction (RSR) introduced geometric prior constraints, utilizing the  $v$ -disparity model and visual odometry to extract elevation information from stereo images. However, these methods struggle in textureless scenes with sparse features and suffer from high computational complexity [8, 10, 11, 39]. Recent advancements based on Neural Radiance Fields (NeRF) have optimized 3D road surface rendering using implicit representations and voxel rendering [32, 42, 47]. Techniques such as plane regularization via Singular Value Decomposition (SVD) have improved NeRF's structural accuracy [42]. Nevertheless, these approaches are sensitive to camera parameters and often prioritize texture over precise elevation data. Some employ mesh partitioning for implicit road surface representation, facilitating large-scale monocular reconstruction [30]. The recent RoadBEV method has shown promise in RSR from a Bird's Eye View (BEV) [55]. However, there remains significant potential for improving processing time and accuracy.

**BEV View Transformation.** Existing BEV view transformation methods can be categorized into three main types: 3D-to-2D projection, 2D-to-3D projection, and fusion projection methods. In 3D-to-2D projection methods, OFT-Net [37] pioneers the use of predefined voxel projections onto images to derive BEV feature representations. Subsequent works [17, 26, 52] build on this approach by employing cross-attention mechanisms within Transformer architectures, though they often overlook depth information during projection, leading to ambiguity. Conversely, 2D-to-3D methods [7, 24, 25, 28, 35], exemplified by LSS [35], project multi-view image features into BEV space based on depth distribution. BEVDepth [25] emphasizes depth supervision, while BEV-Fusion [28] extends the LSS framework into the multi-modal perception domain. Despite these advancements, these methods typically yield relatively sparse BEV features. Recent approaches like FB-BEV [27] and DualBEV [23] aim to integrate both paradigms. However, a unified view transformation method that effectively combines the strengths of both approaches while ensuring suitability for RSR and fast inference speeds remains elusive.

**Deep Learning-Based Stereo Matching.** Stereo matching networks based on deep learning have enhanced disparity estimation accuracy [6, 9, 14, 29, 49, 50]. For instance, PSMNet [6] utilizes spatial pyramid pooling and 3D convolutional neural networks to effectively learn disparity information from stereo images. DispNet [29] employs a correlation layer to directly measure the similarity between left and right images, constructing a single-channel full correlation volume. GWCNet [13] introduces a novel method for creating a 4D cost volume using group-wise correlation. Despite these advancements, these methods often struggle with real-time performance. To address this challenge, some approaches have integrated structures aimed at real-time applications. DeepPruner [9] employs a PatchMatch module to incrementally prune the disparity space for each pixel, thereby reducing computational costs. AANet [51] proposes an intra-scale and cross-scale cost aggregation algorithm as an alternative to traditional 3D convolutions, although this comes with a notable sacrifice in accuracy. Nevertheless, current stereo matching methods still face difficulties in achieving an optimal balance between accuracy and computational efficiency.

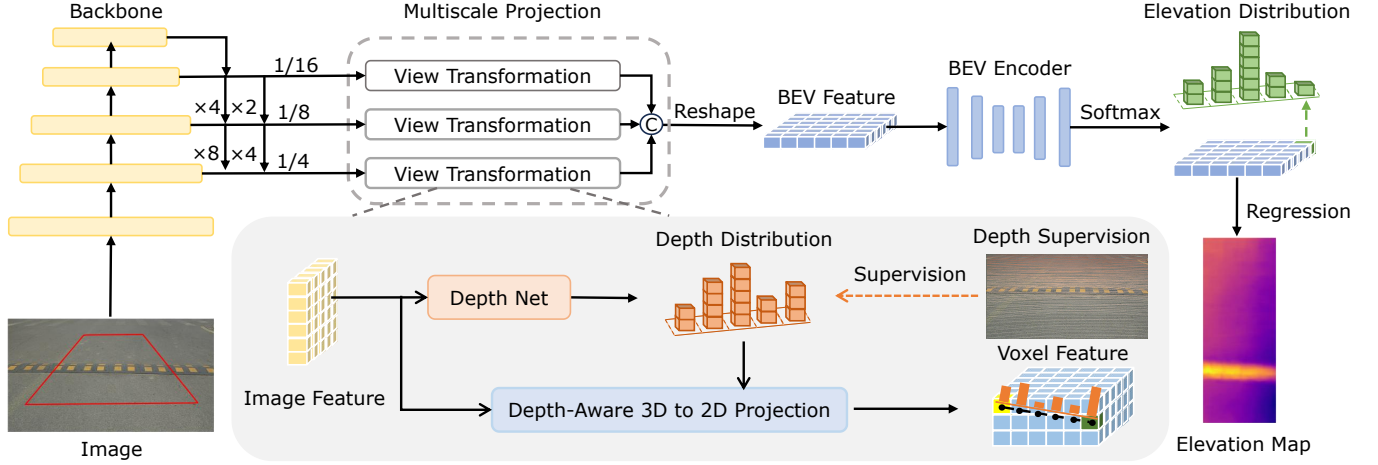


**Figure 2: Overview of FastRSR-mono.** Based on multi-scale image features, we employ Depth-Aware 3D-to-2D Projection (DAP) for multi-scale projection to extract the rich BEV feature. We then use the BEV encoder and a Softmax function to obtain the elevation distribution. Finally, the predicted elevation map is generated by calculating a linear combination of probability scores utilizing shuttle-shaped discretization bins.

### 3 FASTRSR-MONO

In this section, we present the details of FastRSR-mono. We provide an overview of FastRSR-mono in Sec. 3.1. Specifically, to address the limitations of existing view transformation modules for road surface elevation reconstruction, we introduce the Depth-aware 3D-to-2D Projection (DAP) module in Sec. 3.2. Considering the distribution characteristics of road surface elevation, we propose the Shuttle-shape Discretization (SD) strategy in Sec. 3.3.

#### 3.1 Overview of FastRSR-mono

Our goal is to design a novel framework taking image data as input and reconstruct road surface elevation in BEV space. As illustrated in Fig. 2, the monocular image  $I \in \mathbb{R}^{H \times W \times 3}$  is fed into the image backbone MobileNetV2 [38] to obtain multi-scale image features  $F_{img} = \{\mathbb{R}^{\frac{H}{i} \times \frac{W}{i} \times C_i} | i \in [4, 8, 16]\}$ . Then we obtain the predicted depth distributions  $D_{pre} = \{\mathbb{R}^{\frac{H}{i} \times \frac{W}{i} \times C_d} | i \in [4, 8, 16]\}$  by feeding image features into depth net similar to BEVDepth [25]. To ensure the accuracy of depth distribution estimation, we supervise the intermediate depth prediction  $D_{pre}$  using the ground truth depth  $D_{gt}$ . Taking the image feature  $F_{img}$  and depth distribution  $D_{pre}$  as input, the DAP module will efficiently generate the strong voxel feature  $F_{voxel} \in \mathbb{R}^{N_x \times N_y \times N_z \times C_i}$ , as described in Sec. 3.2. Subsequently, we project multi-scale image features via the DAP module and concat the obtained multi-scale voxel features to form a rich voxel feature representation  $\mathbf{B} \in \mathbb{R}^{N_x \times N_y \times N_z \times C}$ , where  $N_x$ ,  $N_y$  and  $N_z$  represent the grid dimensions of the 3D voxel space, and  $C$  is three times  $C_i$ . We reshape the 4D voxel feature  $\mathbf{B}$  into 3D BEV feature  $F_{bev} \in \mathbb{R}^{N_x \times N_y \times (C \times N_z)}$ . We then employ a simplified EfficientNet-B0 [41] as the BEV encoder and a Softmax function to obtain the elevation distribution  $E_{prob} \in \mathbb{R}^{N_x \times N_y \times N}$  over  $N$  shuttle-shape discretization bin-centers  $e_i$ ,  $i = 1, \dots, N$ , where  $N$  is the number of elevation bins. The elevation bin discretization strategy is detailed in Sec. 3.3. Finally, the predicted elevation map  $E_{pre} \in \mathbb{R}^{N_x \times N_y}$  is

calculated from the linear combination of Softmax scores as follows:

$$E_{pre}(x, y) = \sum_{i=1}^N e_i \cdot E_{prob}(x, y, i), \quad (1)$$

where  $x$  and  $y$  represent the lateral and longitudinal coordinates of the BEV grid.

#### 3.2 Depth-Aware 3D-to-2D Projection

Given the image features  $F_{img}$ , we employ a view transformation module to project them into BEV representations. However, current 2D-to-3D projection methods [35] tend to produce sparse BEV features, which suffer from poor elevation information. Additionally, existing 3D-to-2D projection methods [20, 26] utilize a bilinear grid sampler or attention operations to query image features for BEV features, which typically takes much time. Moreover, due to the absence of depth guidance, voxel features are assigned the same value at different elevations along the same ray, which leads to information loss and confusion in elevation reconstruction. To address these challenges, we propose a new and powerful Depth-Aware 3D-to-2D Projection (DAP) module to obtain a stronger BEV representation, which is more suitable for road surface elevation reconstruction. Next, we describe the DAP module in detail.

First, to emphasize variations in road surface profiles, we perform voxel partition within a specific road Region of Interest (ROI). Based on the camera intrinsic and extrinsic parameters  $K$  and  $T$ , we systematically iterate through each voxel cell to calculate the 2D pixel coordinates  $p_{2d} = d \cdot (u, v, 1)$  corresponding to the 3D voxel coordinates  $p_{3d} = (x, y, z)$  as follows:

$$d \cdot (u, v, 1)^T = K \cdot T \cdot (x, y, z)^T, \quad (2)$$

where  $d$  denotes the depth of the 2D pixel point. To distinguish 3D voxels projected onto the same 2D image point along the same ray, we introduce depth information as a key distinguishing factor. Given the image feature  $F_{img}$  and depth distribution  $D_{pre}$ , we employ bilinear grid sampler  $S_{2d}(\cdot)$  and trilinear grid sampler  $S_{3d}(\cdot)$

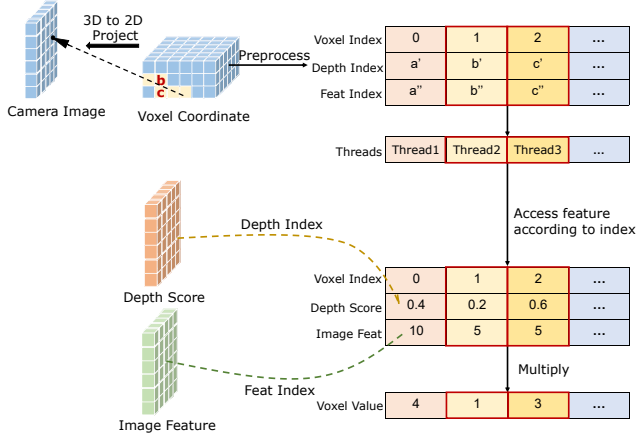


**Figure 3: Depth-Aware 3D-to-2D Projection Module. Despite occupying different elevations, voxels  $b$  and  $c$  share identical features along the same ray. With depth information to assign different weights, these voxels receive distinct values.**

to sample the corresponding image feature and depth probability at the 2D pixel point  $p_{2d}$ . The voxel feature is obtained as follows:

$$F_{\text{voxel}}(p_{3d}) = S_{2d}(F_{\text{img}}, p_{2d}) \cdot S_{3d}(F_d, p_{2d}). \quad (3)$$

Since the projection relationship is established without any learnable parameters, we can accelerate the process by pre-computing the fixed projection indexes according to the established 3D-to-2D projection and storing them in a static look-up table. This allows us to substitute the grid sampler operator. Additionally, we use multiple processing threads to further enhance the speed of this procedure. As illustrated in Fig. 3, we retrieve the value of the corresponding depth scores and feature values using the preprocessed image feature index  $f^{\text{index}}$  and depth index  $d^{\text{index}}$  within the processing thread. By multiplying these values, we derive the voxel feature values as follows:

$$F_{\text{voxel}}(p_{3d}) = F_{\text{img}}(f^{\text{index}}) \cdot F_d(d^{\text{index}}). \quad (4)$$

### 3.3 Shuttle-shape Discretization

The continuous elevation space is discretized into a set of  $N$  bins. Previous elevation discretization is typically performed using Uniform Discretization (UD) with a fixed bin size. However, considering the distribution characteristics of road surface elevation, we propose the Shuttle-shape Discretization (SD) strategy. This approach is centered around a ground elevation value of zero, with bin widths gradually transitioning from dense to sparse towards the upper and lower ends. The elevation discretization techniques are visualized in Fig. 4. SD is defined as follows:

$$b_i = \begin{cases} \left(\frac{N' - N_i}{N'}\right)^\alpha \cdot e_{\text{bound}}, & N_i = 0, 1, \dots, N' - 1 \\ -\left(\frac{N_i - N'}{N'}\right)^\alpha \cdot e_{\text{bound}}, & N_i = N', N' + 1, \dots, N' \end{cases}, \quad (5)$$

$$e_i = \frac{1}{2} \times (b_{i-1} + b_i),$$

where  $b_i$  represents the  $i^{\text{th}}$  elevation bin edge value,  $e_{\text{bound}}$  denotes the boundary of predefined elevation range,  $N' = N/2$  is the half

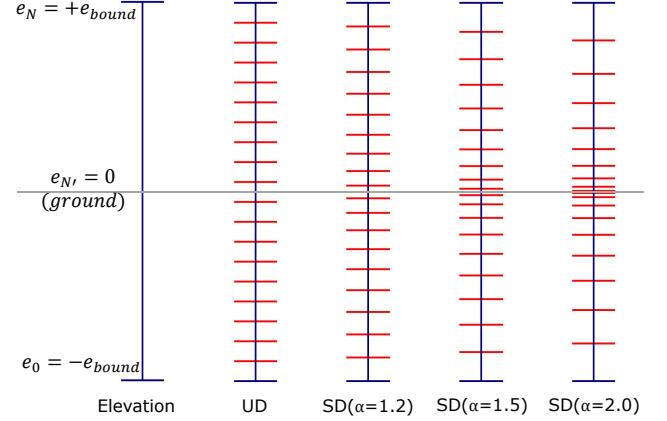


**Figure 4: Discretization bin methods.**

of the number of elevation bins,  $N_i$  denotes the  $i^{\text{th}}$  elevation bin,  $e_i$  is the  $i^{\text{th}}$  elevation bin center value and  $\alpha$  is the hype parameter to control the sensitivity across various elevation ranges, shaping the degree of non-linearity in the output.

## 4 FASTRSR-STEREO

In this section, for stereo images, we present the details of FastRSR-stereo. We begin with an overview of FastRSR-stereo in Sec. 4.1. Specifically, to alleviate the performance loss associated with light-weight architectures, we propose the Spatial Attention Enhancement (SAE) module in Sec. 4.2 and the Confidence Attention Generation (CAG) module in Sec. 4.3.

### 4.1 Overview of FastRSR-stereo

As illustrated in Fig. 5, FastRSR-stereo mainly consists of five components: voxel feature extraction, initial volume construction, attention volume construction, cost aggregation and disparity regression. In the following, we provide an overview of each module.

**Voxel Feature Extraction.** The stereo branch follows a similar paradigm to monocular BEV feature extraction. For a stereo image pair  $I_l, I_r \in \mathbb{R}^{H \times W \times 3}$ , we utilize light backbone MobileNetV2 [38] to obtain image features. Subsequently, we project image features via the Depth-Aware 3D-to-2D Projection (DAP) module to derive rich voxel features  $\mathbf{B}_l, \mathbf{B}_r \in \mathbb{R}^{N_x \times N_y \times N_z \times C}$ .

**Initial Volume Construction.** Given the left and right voxel features  $\mathbf{B}_l$  and  $\mathbf{B}_r$ , we follow the general framework of stereo matching. In the BEV space, the vertical elevation candidate values correspond to disparity values in stereo matching. We construct the initial group-wise correlation cost volume  $\mathbf{V}^{\text{init}}$  [13] as follows:

$$\mathbf{V}^{\text{init}}(x, y, z, g) = \frac{1}{G} \left( \mathbf{B}_l^g(x, y, z) \odot \mathbf{B}_r^g(x, y, z) \right), \quad (6)$$

where  $G = N_c/N_g$ ,  $N_c$  is the number of channels. All the channels are equally divided into  $N_g$  groups along the channel dimension.  $\odot$  represents the element-wise product from the  $g^{\text{th}}$  voxel feature group  $\mathbf{B}_l^g, \mathbf{B}_r^g$ .

**Attention Volume Construction.** We first utilize the Spatial Attention Enhancement (SAE) module to enhance the representation capacity of initial cost volume  $\mathbf{V}^{\text{init}}$ , as detailed in Sec. 4.2.

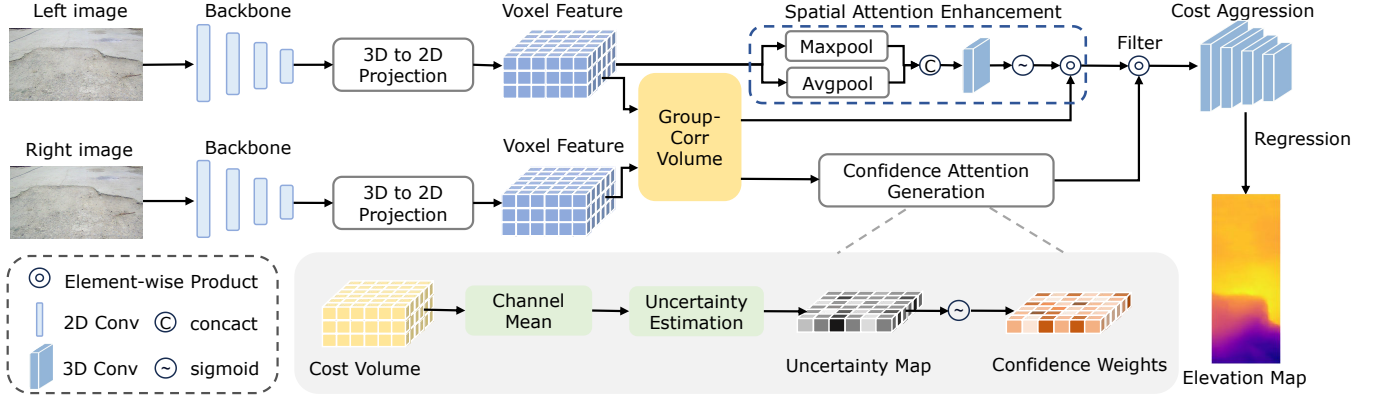


**Figure 5: Overview of FastRSR-stereo.** Following the paradigm of monocular BEV feature extraction, we first construct the initial group-wise correlation cost volume from the left and right voxel features. Subsequently, we introduce the Spatial Attention Enhancement (SAE) module to adaptively enhance important regions, while the Confidence Attention Generation (CAG) module emphasizes high-confidence predictions and suppresses irrelevant information.

Subsequently, we implement the Confidence Attention Generation (CAG) module to derive confidence weights and filter the enhanced cost volume for reliable prediction, as described in Sec. 4.3.

**Cost Aggregation.** We employ an efficient cost aggregation network comprising four initial 3D convolutions followed by three lightweight stacked 3D hourglass networks. Each hourglass module is carefully designed with only three 3D convolutions and a single 3D deconvolution operation.

**Disparity Regression.** With the aggregated volume, the probability of each elevation disparity is calculated via a Softmax operation. The predicted elevation disparity is derived from the linear combination of Softmax scores.

## 4.2 Spatial Attention Enhancement

To mitigate the performance degradation caused by lightweight backbone and cost aggregation networks, we propose the Spatial Attention Enhancement (SAE) module to achieve more accurate matching information with contextual guidance. Inspired by [45], we generate spatial attention weights to effectively and adaptively select important regions. Next, we explain our SAE module in detail.

Given the left voxel feature  $\mathbf{B}_l \in \mathbb{R}^{N_x \times N_y \times N_z \times C}$ , we first apply max pooling and average pooling operations along the channel dimension to obtain pooling maps  $\mathbf{B}_{avg}, \mathbf{B}_{max} \in \mathbb{R}^{N_x \times N_y \times N_z \times 1}$ . We then concatenate these maps to form a map in  $\mathbb{R}^{N_x \times N_y \times N_z \times 2}$ . Subsequently, to derive the spatial attention weights  $\mathbf{A}^s$ , we perform a convolution operation and a Sigmoid function as follows:

$$\mathbf{A}^s = \sigma \left( f^{7 \times 7} ([Avg(\mathbf{B}_l); Max(\mathbf{B}_l)]) \right), \quad (7)$$

where  $\sigma$  denotes the Sigmoid function and  $f^{7 \times 7}$  represents a 3D convolution operation with the filter size of  $1 \times 7 \times 7$ . The spatial attention weights encode where to be emphasized or suppressed, allowing for the adaptive selection of important regions. The enhanced cost volume  $\mathbf{V}^e$  is computed as follows:

$$\mathbf{V}^e = \mathbf{A}^s \odot \mathbf{V}^{init}. \quad (8)$$

## 4.3 Confidence Attention Generation

Despite the effectiveness of the spatial attention enhancement module, we argue that how to design an effective attention generation module for emphasizing high-confidence predictions while suppressing irrelevant information remains crucial. For stereo estimation in BEV space, we obtain the elevation value of a BEV grid by identifying the most similar matching points among the elevation candidates of left and right voxel features along the vertical dimension. The ideal elevation distribution within a grid should be unimodal, peaking at correctly matched points. Grids with a multimodal distribution are considered unreliable. To emphasize high-confidence predictions, we propose the Confidence Attention Generation (CAG) module.

Given the initial cost volume  $\mathbf{V}^{init} \in \mathbb{R}^{N_g \times N_x \times N_y \times N_z}$ , we first compute the average value across all channels. Then we obtain the elevation probability distribution volume  $\mathbf{P}^{init} \in \mathbb{R}^{N_x \times N_y \times N_z}$  by applying the Softmax function. We regress the elevation disparity map  $\mathbf{D}^{init} \in \mathbb{R}^{N_x \times N_y}$  from the linear combination of probabilities  $\mathbf{P}^{init}$ . The uncertainty is calculated from the variance of the elevation distribution as follows:

$$U(i) = \sum_{j=0}^{N_z-1} \left( z_j - \mathbf{D}^{init}(i) \right)^2 \times \mathbf{P}_j^{init}(i), \quad (9)$$

where  $z_j$  is the  $j^{th}$  voxel elevation center and  $\mathbf{P}_j^{init}(i)$  represents the  $j^{th}$  probability value at the BEV grid  $i$ . The confidence  $\mathbf{A}^c$  at the grid  $i$  is defined as follows:

$$\mathbf{A}^c(i) = \sigma(\epsilon + s \times U(i)), \quad (10)$$

where  $s, \epsilon$  are learnable parameters, and  $\sigma$  denotes the Sigmoid function. The confidence attention weights  $\mathbf{A}^c \in \mathbb{R}^{N_x \times N_y}$  indicate that BEV grids with high confidence correspond to reliable identification of a unique match. Finally, the attention volume  $\mathbf{V}^a$  is computed as follows:

$$\mathbf{V}^a = \mathbf{A}^c \odot \mathbf{V}^e. \quad (11)$$

## 5 TRAINING STRATEGY

Our method adopts an end-to-end training strategy, supervising the intermediate predictions of depth distribution and the final predicted elevation. The ground truth values for depth and elevation are derived from LiDAR point clouds, providing a robust and accurate foundation for training. We employ the cross entropy losses to train the network, our final total loss is defined as:

$$\begin{aligned} \mathcal{L} = & \frac{1}{N_{grid}} \sum_{i=1}^{N_{grid}} M_e(i) \cdot CE(E_{pre}(i), E_{gt}(i)) \\ & + \beta \cdot \frac{1}{N_{grid}} \sum_{i=1}^{N_{grid}} M_d(i) \cdot CE(D_{pre}(i), D_{gt}(i)), \end{aligned} \quad (12)$$

where  $N_{grid} = N_x \times N_y$  is the number of BEV grids,  $E_{pre}$  denotes the predicted elevation,  $E_{gt}$  represents the Ground-Truth (GT) elevation value,  $D_{pre}$  is depth distribution predictions and  $D_{gt}$  is depth distribution labels. To ensure the accuracy of our predictions, we utilize the binary GT masks  $M_e$  and  $M_d$  to filter valid elevation and depth values. We set  $\beta = 0.25$  for all experiments, which balances the contributions of elevation and depth losses in our total loss.

## 6 EXPERIMENT

### 6.1 Experimental Setup

**Dataset and Metrics.** The RSRD dataset is the large-scale and real-world dataset for road surface reconstruction [54]. It provides 2,800 pairs of high-resolution stereo images, dense point cloud labels, and motion pose information within a dense subset. For training our network, we utilize a representative subset containing 1,210 training samples and 371 testing samples. In evaluations, we use the metrics defined as: Absolute Error (Abs. err.):  $\frac{1}{N_{grid}} \sum_{i=1}^{N_{grid}} |E_{gt}(i) - E_{pre}(i)|$ , Root Mean Squared Error (RMSE):  $\sqrt{\frac{1}{N_{grid}} \sum_{i=1}^{N_{grid}} (E_{gt}(i) - E_{pre}(i))^2}$ , the percentage of grids with error greater than 0.5 cm ( $>0.5$  cm), and the GPU latency in inference.

**Implementation Details.** We implement the proposed network operating at a cropped image resolution of  $960 \times 528$  in PyTorch. For depth-aware 3D-to-2D projection, we define the ROI as  $[-1.0m, 0.9m]$ ,  $[2.2m, 7.1m]$  and  $[-0.2m, 0.2m]$  with a voxel resolution of  $[x_{res}, y_{res}, z_{res}] = [0.03m, 0.03m, 0.01m]$  along X, Y, Z axes. Our model is trained for 50 epochs using a batch size of 8 across all experiments. We utilize the AdamW optimizer with a weight decay  $1e-4$ , coupled with OneCycleLR scheduling. The maximum learning rate is set to  $8e-4$  for FastRSR-mono, while  $5e-4$  for FastRSR-stereo with a linear decreasing strategy. All latency tests are conducted on a single NVIDIA 3090 GPU.

### 6.2 Comparisons with State-of-the-art

We comprehensively compare our proposed models with the baseline method RoadBEV [55], several state-of-the-art monocular depth estimation and stereo matching approaches. For a fair comparison, these models follow their original training configurations to obtain depth from the perspective view, which is then converted into BEV to generate the elevation map.

**Evaluation on Monocular Elevation Estimation.** We compared our FastRSR-mono model with four baseline monocular depth

**Table 1: Performance comparison on the RSRD dataset.**

Method		Abs. err. (cm)	RMSE (cm)	>0.5 cm (%)	Latency (ms)
Mono	PixelFormer [1]	2.65	2.86	82.0	23.3
	iDisc [36]	2.64	2.88	84.3	81.3
	AdaBins [4]	2.59	2.79	82.4	46.5
	RoadBEV-mono [55]	1.83	2.07	78.6	37.3
	<b>FastRSR-mono</b>	<b>1.72</b>	<b>1.95</b>	<b>76.3</b>	<b>15.1</b>
Stereo	IGEV-Stereo[49]	0.651	0.797	49.5	217.5
	PSMNet [6]	0.654	0.785	50.1	86.2
	ACVNet [50]	0.596	0.723	46.2	83.3
	GwcNet [13]	0.588	0.711	44.9	64.1
	RoadBEV-stereo [55]	0.503	0.609	37.0	125.0
	<b>FastRSR-stereo</b>	<b>0.495</b>	<b>0.605</b>	<b>36.8</b>	<b>21.4</b>

estimation methods using the RSRD dataset in Tab. 1. The results lead us to two key conclusions: (1) *Significant Performance Improvement.* FastRSR-mono achieves a state-of-the-art absolute error (Abs. err.) of 1.72 cm, which surpasses PixelFormer [1] by 35.1%. This significant improvement highlights the effectiveness of our model in monocular elevation reconstruction. (2) *Rapid Inference Efficiency.* FastRSR-mono model achieves an inference time of only 15.1 ms, which is substantially lower than other methods, making our monocular model a practical choice for dynamic environments.

**Evaluation on Stereo Elevation Estimation.** We compared our FastRSR-stereo model with five baseline stereo matching methods using the RSRD dataset in Tab. 1. The results lead us to three key conclusions: (1) *Superior Accuracy Compared with Monocular Methods.* It is evident that stereo matching models generally outperform monocular approaches. Notably, our proposed FastRSR-stereo model exhibits significant advantages, achieving the absolute elevation error of 0.495 cm, the lowest among the evaluated stereo methods. (2) *Real-time Performance.* The inference time for FastRSR-stereo is 21.4 ms, which surpasses existing stereo competitors by at least  $3.0\times$  speedup. (3) *Limited Accuracy Improvement.* While stereo methods generally outperform monocular ones, the accuracy gains are marginal. A potential reason is that the models already reach very high accuracy, while making further promotion is challenging. Additionally, noise in the labels could hinder further enhancements.

### 6.3 Ablation Studies for FastRSR-mono

**Contribution of major components in FastRSR-mono.** To verify the effectiveness of our proposed modules, we take RoadBEV-mono [55] with a light backbone [38] as our baseline. We conduct an ablation study on the components in FastRSR-mono and summarize our results in Tab. 2. We evaluate model variants using different combinations of the proposed modules, including Shuttle-shape Discretization (SD), Multi-Scale Projection (MSP) and Depth-Aware 3D-to-2D Projection (DAP).

We first investigate the effect of each component. In model variants (a), (b), and (c), we add different modules separately. The experimental results show that all model variants get improved performance compared to the baseline, verifying the effectiveness of the proposed modules. Moreover, the results of model variants (d), (e), and (f) prove that different modules are complementary to each other. Finally, using all the proposed modules together, we arrive

**Table 2: Ablation study on the components in FastRSR-mono. SD is the shuttle-shape discretization. MSP means using the multi-scale projection. DAP denotes the depth-aware 3D-to-2D projection module.**

Setting	SD	MSP	DAP	Abs. err. (cm)	RMSE (cm)	>0.5 cm (%)	Latency (ms)
Baseline	✗	✗	✗	2.22	2.50	83.0	14.2
a	✓	✗	✗	1.87	2.10	77.5	14.2
b	✗	✓	✗	1.94	2.16	78.2	14.9
c	✗	✗	✓	1.91	2.16	78.1	14.2
d	✓	✓	✗	1.80	2.01	76.4	14.9
e	✗	✓	✓	1.82	2.07	77.1	15.1
f	✓	✗	✓	1.76	1.98	76.2	14.2
g	✓	✓	✓	<b>1.72</b>	<b>1.95</b>	<b>76.3</b>	<b>15.1</b>

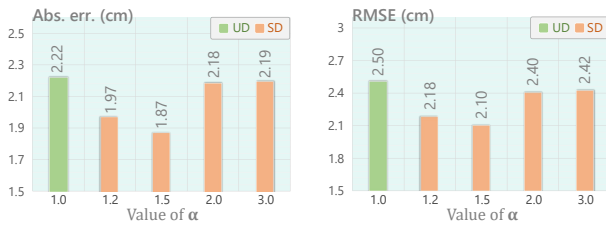


**Figure 6: Comparison of different discretization bin methods.**

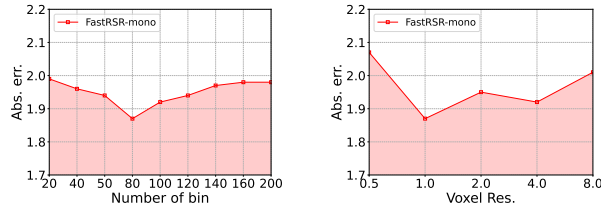


**Figure 7: Effect of numbins. Figure 8: Effect of voxel res.**

at the full FastRSR-mono, which achieves the best performance of 1.72 cm, significantly surpassing the baseline of 22.5%.

**Discretization Bin Types.** To evaluate the performance of different discretization bin methods, we perform an ablation study in Fig. 6. The Shuttle-shape Discretization (SD) demonstrates superior adaptability to real-world road geometry compared to Uniform Discretization (UD). When our SD strategy with  $\alpha = 1.5$  is applied instead of UD, the prediction accuracy improves 15%. The performance degradation when  $\alpha = 2.0$  reveals that excessive focus on near-field details introduces noise amplification in distant areas. Ultimately, the performance achieves the best 1.87 cm absolute elevation error and 2.10 cm root mean square error at  $\alpha = 1.5$ .

**Number of Bins ( $N$ ).** To thoroughly evaluate the effect of different numbers of bins, we conduct a detailed ablation study across varying bin counts as shown in Fig. 7. When  $N$  increases from 20 to 80, we observe a consistent decrease in absolute elevation error, which indicates improved elevation discrimination with finer quantization. However, beyond  $N = 80$ , the performance declines by 3% to 6%. This degradation is attributed to over-discretization, where excessive binning results in sparse statistics per bin, increasing sensitivity to noise. So we select  $N = 80$  for our final model.

**Voxel Vertical Resolutions.** To investigate the effect of different vertical resolutions of the voxel, we conduct a comprehensive

**Table 3: Comparison of multi-scale projection designs.**

Method		Abs. err. (cm)	RMSE (cm)	>0.5 cm (%)	Latency (ms)
MS Image to MS BEV	plus	1.81	2.04	77.0	15.1
	concat	1.84	2.09	77.0	15.5
MS Image to SS BEV	plus	1.83	2.06	76.4	<b>14.6</b>
	<b>concat</b>	<b>1.80</b>	<b>2.01</b>	<b>76.4</b>	14.9

**Table 4: Comparison of view transformation types.**

View Transformation	Abs. err. (cm)	RMSE (cm)	>0.5 cm (%)	Latency (ms)
Bilinear-Sampling [20]	1.80	2.02	76.4	4.21
Look-Up Table [55]	1.80	2.01	76.4	0.44
LSS [25]	1.85	2.06	76.5	0.46
<b>DAP</b>	<b>1.72</b>	<b>1.95</b>	<b>76.3</b>	<b>0.05</b>

ablation study as shown in Fig. 8. Overly fine 0.5 cm resolution leads to an absolute error of 2.07 cm, which significantly increases the likelihood of adjacent voxels projecting onto the same image location, complicating the distinction of subtle differences. Moreover, the 1.0 cm resolution emerges as the optimal choice, reducing the absolute error by 10%. While coarser resolutions ranging from 2.0 to 8.0 cm progressively lose terrain details. At the 8.0 cm resolution, we observe a 3% increase in absolute error, making it challenging to accurately represent elevation features with rich information.

**Multi-Scale Projection.** To validate the performance of different multi-scale projection designs, we carefully compare four distinct configurations: Multi-Scale (MS) image projection to MS BEV or Single-Scale (SS) BEV, and various fusion methods of multiple BEV maps including concatenation or addition. As shown in Tab. 3, the MS-to-SS BEV projection outperforms MS-to-MS approaches because the SS BEV representation maintains better spatial consistency, avoiding the feature misalignment and information redundancy. Notably, when employing MS image projection to MS BEV with concatenation, we achieve an optimal trade-off with the absolute elevation error of 1.80 cm and latency of 14.9 ms.

**View Transformation Types.** As shown in Tab. 4, we compare different view transformation operations under the same training settings. When using the look-up table [55] instead of bilinear-sampling [20] 3D-to-2D projection, the inference time significantly decreases by 89.5%. When applying the LSS method [25] for 2D-to-3D projection alongside the look-up table, we experience a slight decrease in accuracy with the absolute elevation error of 1.85 cm, which may be attributed to the limitations imposed by the sparse BEV elevation features. The DAP module incorporates depth information and CUDA acceleration operators [21], achieving optimal accuracy of 1.72 cm absolute elevation error and the shortest inference time of 0.05 ms, which is over 8 times faster than other methods. Overall, these findings highlight the effective and efficient capabilities of our DAP method in view transformation tasks, demonstrating its potential for enhancing both accuracy and speed.

## 6.4 Ablation Studies for FastRSR-stereo

**Contribution of major components in FastRSR-stereo.** We evaluate the effectiveness of individual components in FastRSR-stereo. We establish our base model on RoadBEV-stereo [55]. The

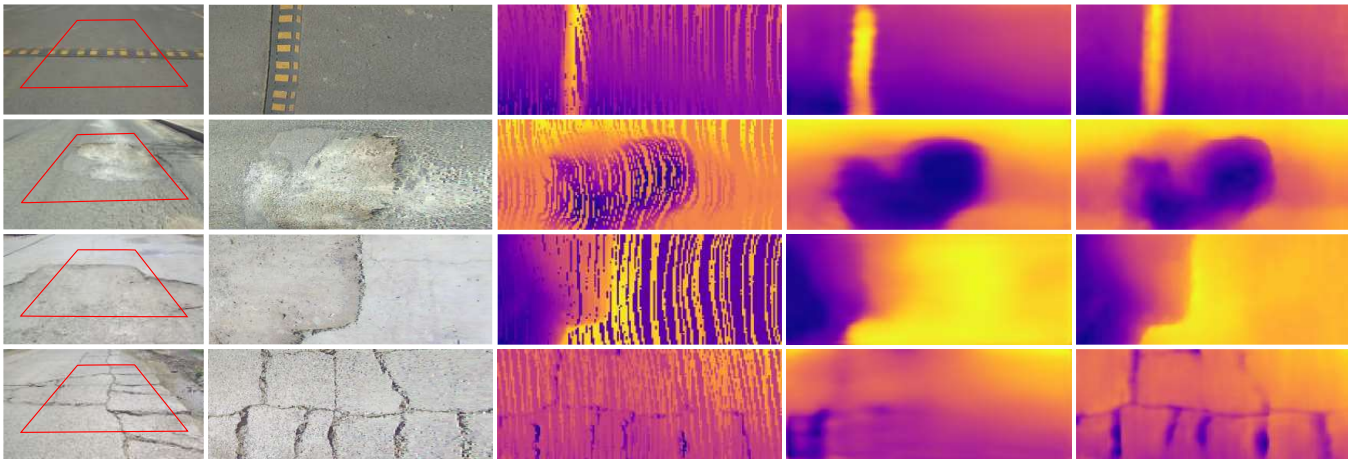


Figure 9: Qualitative results on RSRD. From left to right: left images, transformed images in BEV space, ground-truth elevation maps, estimated elevation maps by FastRSR-mono and estimated elevation maps by FastRSR-stereo.

Table 5: Ablation study on the components in FastRSR-stereo. GC represents the group-wise correlation cost volume construction. SAE means using spatial attention enhancement. CAG denotes the confidence attention generation module.

Setting	GC	SAE	CAG	Abs. err. (cm)	RMSE (cm)	>0.5 cm (%)	Latency (ms)
Baseline	✗	✗	✗	0.539	0.662	40.8	28.4
a	✓	✗	✗	0.524	0.633	39.7	18.2
b	✓	✓	✗	0.509	0.614	38.1	20.1
c	✓	✗	✓	0.503	0.613	37.2	19.1
d	✓	✓	✓	<b>0.495</b>	<b>0.605</b>	<b>36.8</b>	<b>21.4</b>

Table 6: Comparison of different cost volume constructions.

Method	Abs. err. (cm)	RMSE (cm)	>0.5 cm (%)	Latency (ms)
Diff	0.539	0.662	40.8	28.4
Multiply	<b>0.518</b>	0.635	39.7	28.5
Group-Diff	0.545	0.670	40.5	18.2
<b>Group-Corr</b>	0.524	<b>0.633</b>	<b>39.7</b>	<b>18.2</b>

architecture incorporates a lightweight cost aggregation network and follows a similar paradigm to our previously established monocular BEV feature extraction module, which employs light backbone MobileNetV2 [38] to obtain image features and project image features via the DAP module to derive voxel features.

As shown in Tab. 5, all the modules are beneficial to the performance gains. Using the GC module can lead to a 35.9% decrease in GPU latency in (a). Subsequently, we employ the SAE module for the adaptive selection of important regions, resulting in 2.8% absolute elevation error decrease in (b). By incorporating the CAG module for reliable prediction, our model achieves 4.0% decrease in absolute error in (c). Finally, the complete model reaches the best performance, with an 8.16% improvement in the absolute elevation error and a 24.6% decrease in inference time.

**Cost Volume Construction Methods.** To investigate the effect of different cost volume construction methods, we conduct a comprehensive ablation study as shown in Tab. 6. We observe that

the inference time is significantly decreased when constructing the group-corr type. This significant speed improvement stems from the parallel group-wise computation. Notably, the group-corr type exhibits only a slight 1% increase in the absolute elevation error compared to the multiply type. This is negligible compared to the significant 36% decrease in inference time it brings. The group-corr method demonstrates optimal performance.

## 6.5 Qualitative evaluation

Fig. 9 illustrates the performance of FastRSR models in reconstructing road surface elevation based on monocular or stereo images. In the first scenario with a speed bump, both models effectively capture distinct contours and elevation variations. In the second and third scenarios, which feature significant depressions and potholes, the two models accurately capture the variations in elevation. In the final scenario, where the elevation changes are less pronounced, the FastRSR-stereo model still reveals details of cracks and uneven areas, while the FastRSR-mono model produces a rougher reconstruction. Moreover, the performance is less remarkable at greater distances due to challenges in capturing fine details and potential noise in labels. Overall, this demonstrates the robust reconstruction capabilities of our model across various road surface conditions, confirming its effectiveness for road surface analysis.

## 7 CONCLUSIONS

In this paper, we propose two efficient and accurate models: FastRSR-mono and FastRSR-stereo. To address the limitations of existing view transformation modules for road surface elevation reconstruction, we introduce the Depth-Aware 3D-to-2D Projection (DAP) module, which effectively queries depth and image features to aggregate strong BEV features. To mitigate accuracy loss in the lightweight stereo architectures, we first present the Spatial Attention Enhancement (SAE) module to adaptively select important information. Then, we propose Confidence Attention Generation (CAG) module to highlight high-confidence predictions. Our model demonstrates state-of-the-art performance, enabling efficient and accurate road surface elevation reconstruction.

## REFERENCES

- [1] Ashutosh Agarwal and Chetan Arora. 2023. Attention attention everywhere: Monocular depth prediction with skip attention. In *Proceedings of the IEEE/CVF Winter Conference on Applications of Computer Vision*. 5861–5870.
- [2] A Alrajhi, K Roy, L Qingge, and J Kribs. 2023. Detection of road condition defects using multiple sensors and IoT technology: A review. *IEEE Open Journal of Intelligent Transportation Systems* 4 (2023), 372–392.
- [3] Amir Beketov and Shakhnoza Khalimova. 2023. Impact of roughness and friction properties of road surface of urban streets on the traffic safety. *COMMUNICATIONS* 25, 3 (2023), F51–F63.
- [4] Shariq Farooq Bhat, Ibraheem Alhashim, and Peter Wonka. 2021. Adabins: Depth estimation using adaptive bins. In *Proceedings of the IEEE/CVF conference on computer vision and pattern recognition*. 4009–4018.
- [5] Andrew Blake, Pushmeet Kohli, and Carsten Rother. 2011. *Markov random fields for vision and image processing*. MIT press.
- [6] Jia-Ren Chang and Yong-Sheng Chen. 2018. Pyramid stereo matching network. In *Proceedings of the IEEE conference on computer vision and pattern recognition*. 5410–5418.
- [7] Zhuo Chen, Haimei Zhao, Xiaoshuai Hao, Bo Yuan, and Xiu Li. 2025. STViT+: improving self-supervised multi-camera depth estimation with spatial-temporal context and adversarial geometry regularization. *Applied Intelligence* 55, 5 (2025), 328.
- [8] Han-Cheng Dan, Bingjie Lu, and Mengyu Li. 2024. Evaluation of asphalt pavement texture using multiview stereo reconstruction based on deep learning. *Construction and Building Materials* 412 (2024), 134837.
- [9] Shivam Duggal, Shenlong Wang, Wei-Chiu Ma, Rui Hu, and Raquel Urtasun. 2019. Deeppruner: Learning efficient stereo matching via differentiable patchmatch. In *Proceedings of the IEEE/CVF international conference on computer vision*. 4384–4393.
- [10] Rui Fan, Xiao Ai, and Naim Dahnoun. 2018. Road surface 3D reconstruction based on dense subpixel disparity map estimation. *IEEE Transactions on Image Processing* 27, 6 (2018), 3025–3035.
- [11] Rui Fan, Jianhao Jiao, Jie Pan, Huaiyang Huang, Shaojie Shen, and Ming Liu. 2019. Real-Time Dense Stereo Embedded in a UAV for Road Inspection. In *2019 IEEE/CVF Conference on Computer Vision and Pattern Recognition Workshops (CVPRW)*. IEEE, 535–543.
- [12] Jenny Guo, Meng-Ju Tsai, and Jen-Yu Han. 2015. Automatic reconstruction of road surface features by using terrestrial mobile lidar. *Automation in Construction* 58 (2015), 165–175.
- [13] Xiaoyang Guo, Kai Yang, Wukui Yang, Xiaogang Wang, and Hongsheng Li. 2019. Group-wise correlation stereo network. In *Proceedings of the IEEE/CVF conference on computer vision and pattern recognition*. 3273–3282.
- [14] Xianda Guo, Chenming Zhang, Dujun Nie, Wenzhao Zheng, Youmin Zhang, and Long Chen. 2024. LightStereo: Channel Boost Is All Your Need for Efficient 2D Cost Aggregation. *arXiv preprint arXiv:2406.19833* (2024).
- [15] Xiaoshuai Hao, Yunfeng Diao, Mengchuan Wei, Yifan Yang, Peng Hao, Rong Yin, Hui Zhang, Weiming Li, Shu Zhao, and Yu Liu. 2025. MapFusion: A novel BEV feature fusion network for multi-modal map construction. *Information Fusion* 119 (2025), 103018.
- [16] Xiaoshuai Hao, Ruikai Li, Hui Zhang, Dingzhe Li, Rong Yin, Sangil Jung, Seung-In Park, ByungIn Yoo, Haimei Zhao, and Jing Zhang. 2024. MapDistill: Boosting Efficient Camera-based HD Map Construction via Camera-LiDAR Fusion Model Distillation. *arXiv preprint arXiv:2407.11682* (2024).
- [17] Xiaoshuai Hao, Guanqun Liu, Yuting Zhao, Yuheng Ji, Mengchuan Wei, Haimei Zhao, Lingdong Kong, Rong Yin, and Yu Liu. 2025. MSC-Bench: Benchmarking and Analyzing Multi-Sensor Corruption for Driving Perception. *arXiv preprint arXiv:2501.01037* (2025).
- [18] Xiaoshuai Hao, Mengchuan Wei, Yifan Yang, Haimei Zhao, Hui Zhang, Yi Zhou, Qiang Wang, Weiming Li, Lingdong Kong, and Jing Zhang. 2024. Is Your HD Map Constructor Reliable under Sensor Corruptions? *arXiv preprint arXiv:2406.12214* (2024).
- [19] Xiaoshuai Hao, Hui Zhang, Yifan Yang, Yi Zhou, Sangil Jung, Seung-In Park, and ByungIn Yoo. 2024. MbFusion: A new multi-modal bev feature fusion method for hd map construction. In *2024 IEEE International Conference on Robotics and Automation (ICRA)*. IEEE, 15922–15928.
- [20] Adam W Harley, Zhaoyuan Fang, Jie Li, Rares Ambrus, and Katerina Fragkiadaki. 2023. Simple-bev: What really matters for multi-sensor bev perception?. In *2023 IEEE International Conference on Robotics and Automation (ICRA)*. IEEE, 2759–2765.
- [21] Junjie Huang and Guan Huang. 2022. Bevpoolv2: A cutting-edge implementation of bevnet toward deployment. *arXiv preprint arXiv:2211.17111* (2022).
- [22] Junjie Huang, Guan Huang, Zheng Zhu, Yun Ye, and Dalong Du. 2021. BevDet: High-performance multi-camera 3d object detection in bird-eye-view. *arXiv preprint arXiv:2112.11790* (2021).
- [23] Peidong Li, Wancheng Shen, Qihao Huang, and Dixiao Cui. 2024. DualBEV: CNN is All You Need in View Transformation. *arXiv preprint arXiv:2403.05402* (2024).
- [24] Yinhao Li, Han Bao, Zheng Ge, Jinrong Yang, Jianjian Sun, and Zeming Li. 2023. Bevstereo: Enhancing depth estimation in multi-view 3d object detection with temporal stereo. In *Proceedings of the AAAI Conference on Artificial Intelligence*, Vol. 37. 1486–1494.
- [25] Yinhao Li, Zheng Ge, Guanyi Yu, Jinrong Yang, Zengran Wang, Yukang Shi, Jianjian Sun, and Zeming Li. 2023. Bevdepth: Acquisition of reliable depth for multi-view 3d object detection. In *Proceedings of the AAAI Conference on Artificial Intelligence*, Vol. 37. 1477–1485.
- [26] Zhiqi Li, Wenhai Wang, Hongyang Li, Enze Xie, Chonghao Sima, Tong Lu, Yu Qiao, and Jifeng Dai. 2022. Bevformer: Learning bird's-eye-view representation from multi-camera images via spatiotemporal transformers. In *European conference on computer vision*. Springer, 1–18.
- [27] Zhiqi Li, Zhiding Yu, Wenhai Wang, Anima Anandkumar, Tong Lu, and Jose M Alvarez. 2023. Fb-bev: Bev representation from forward-backward view transformations. In *Proceedings of the IEEE/CVF International Conference on Computer Vision*. 6919–6928.
- [28] Zhijian Liu, Haotian Tang, Alexander Amini, Xinyu Yang, Huizi Mao, Daniela L Rus, and Song Han. 2023. Bevfusion: Multi-task multi-sensor fusion with unified bird's-eye view representation. In *2023 IEEE international conference on robotics and automation (ICRA)*. IEEE, 2774–2781.
- [29] Nikolaus Mayer, Eddy Ilg, Philip Hausser, Philipp Fischer, Daniel Cremers, Alexey Dosovitskiy, and Thomas Brox. 2016. A large dataset to train convolutional networks for disparity, optical flow, and scene flow estimation. In *Proceedings of the IEEE conference on computer vision and pattern recognition*. 4040–4048.
- [30] Ruohong Mei, Wei Sui, Jiaxin Zhang, Xue Qin, Gang Wang, Tao Peng, Tao Chen, and Cong Yang. 2024. Rome: Towards large scale road surface reconstruction via mesh representation. *IEEE Transactions on Intelligent Vehicles* 9 (2024), 5173–5185.
- [31] Georgios-Tsmpikos Michailidis, Renato Pajarola, and Ioannis Andreadis. 2013. High performance stereo system for dense 3-D reconstruction. *IEEE transactions on circuits and systems for video technology* 24, 6 (2013), 929–941.
- [32] Ben Mildenhall, Pratul P Srinivasan, Matthew Tancik, Jonathan T Barron, Ravi Ramamoorthi, and Ren Ng. 2021. Nerf: Representing scenes as neural radiance fields for view synthesis. *Commun. ACM* 65, 1 (2021), 99–106.
- [33] Tao Ni, Wenhao Li, Dingxuan Zhao, and Zhifei Kong. 2020. Road profile estimation using a 3D sensor and intelligent vehicle. *Sensors* 20, 13 (2020), 3676.
- [34] Florin Oniga and Sergiu Nedevschi. 2009. Processing dense stereo data using elevation maps: Road surface, traffic isle, and obstacle detection. *IEEE Transactions on Vehicular Technology* 59, 3 (2009), 1172–1182.
- [35] Jonah Philion and Sanja Fidler. 2020. Lift, splat, shoot: Encoding images from arbitrary camera rigs by implicitly unprojecting to 3d. In *Computer Vision—ECCV 2020: 16th European Conference, Glasgow, UK, August 23–28, 2020, Proceedings, Part XIV* 16. Springer, 194–210.
- [36] Luigi Piccinelli, Christos Sakaridis, and Fisher Yu. 2023. idisc: Internal discretization for monocular depth estimation. In *Proceedings of the IEEE/CVF Conference on Computer Vision and Pattern Recognition*. 21477–21487.
- [37] Thomas Roddick, Alex Kendall, and Roberto Cipolla. 2019. Orthographic Feature Transform for Monocular 3D Object Detection. *British Machine Vision Conference* (2019), 2–3.
- [38] Mark Sandler, Andrew Howard, Menglong Zhu, Andrey Zhmoginov, and Liang-Chieh Chen. 2018. Mobilenetv2: Inverted residuals and linear bottlenecks. In *Proceedings of the IEEE conference on computer vision and pattern recognition*. 4510–4520.
- [39] Johannes L Schönberger, Enliang Zheng, Jan-Michael Frahm, and Marc Pollefeys. 2016. Pixelwise view selection for unstructured multi-view stereo. In *Computer Vision—ECCV 2016: 14th European Conference, Amsterdam, The Netherlands, October 11–14, 2016, Proceedings, Part III* 14. Springer, 501–518.
- [40] Faranak Shamsafar, Samuel Woerz, Rafia Rahim, and Andreas Zell. 2022. Mobilestereonet: Towards lightweight deep networks for stereo matching. In *Proceedings of the IEEE/CVF winter conference on applications of computer vision*. 2417–2426.
- [41] Mingxing Tan and Quoc V. Le. 2019. EfficientNet: Rethinking Model Scaling for Convolutional Neural Networks. In *Proceedings of the International Conference on Machine Learning*. PMLR, Long Beach, CA, USA, 6105–6114.
- [42] Fusang Wang, Arnaud Louys, Nathan Piasco, Moussab Bennehar, Luis Roldão, and Dzmitry Tsishkou. 2023. Planerf: Svd unsupervised 3d plane regularization for nerf large-scale scene reconstruction. *arXiv preprint arXiv:2305.16914* (2023).
- [43] Lili Wang, Dingxuan Zhao, Tao Ni, and Shuang Liu. 2020. Extraction of preview elevation information based on terrain mapping and trajectory prediction in real-time. *IEEE Access* 8 (2020), 76618–76631.
- [44] Qiang Wang, Shaohuai Shi, Shizhen Zheng, Kaiyong Zhao, and Xiaowen Chu. 2020. Fadnet: A fast and accurate network for disparity estimation. In *2020 IEEE international conference on robotics and automation (ICRA)*. IEEE, 101–107.
- [45] Sanghyun Woo, Jongchan Park, Joon-Young Lee, and In So Kweon. 2018. Cbam: Convolutional block attention module. In *Proceedings of the European conference on computer vision (ECCV)*. 3–19.
- [46] Enze Xie, Zhiding Yu, Daquan Zhou, Jonah Philion, Anima Anandkumar, Sanja Fidler, Ping Luo, and Jose M Alvarez. 2022. M2BEV: Multi-Camera Joint 3D Detection and Segmentation with Unified Birds-Eye View Representation. *arXiv preprint arXiv:2204.05088* (2022).

- [47] Ziyang Xie, Ziqi Pang, and Yu-Xiong Wang. 2023. Mv-map: Offboard hd-map generation with multi-view consistency. In *Proceedings of the IEEE/CVF International Conference on Computer Vision*. 8658–8668.
- [48] Yi Xin, Siqi Luo, Haodi Zhou, Junlong Du, Xiaohong Liu, Yue Fan, Qing Li, and Yuntao Du. 2024. Parameter-efficient fine-tuning for pre-trained vision models: A survey. *arXiv preprint arXiv:2402.02242* (2024).
- [49] Gangwei Xu, Xianqi Wang, Xiaohuan Ding, and Xin Yang. 2023. Iterative geometry encoding volume for stereo matching. In *Proceedings of the IEEE/CVF Conference on Computer Vision and Pattern Recognition*. 21919–21928.
- [50] Gangwei Xu, Yun Wang, Junda Cheng, Jinhui Tang, and Xin Yang. 2023. Accurate and efficient stereo matching via attention concatenation volume. *IEEE Transactions on Pattern Analysis and Machine Intelligence* 46, 4 (2023), 2461–2474.
- [51] Haofei Xu and Juyong Zhang. 2020. Aanet: Adaptive aggregation network for efficient stereo matching. In *Proceedings of the IEEE/CVF conference on computer vision and pattern recognition*. 1959–1968.
- [52] Chenyu Yang, Yuntao Chen, Hao Tian, Chenxin Tao, Xizhou Zhu, Zhaoxiang Zhang, Gao Huang, Hongyang Li, Yu Qiao, Lewei Lu, et al. 2023. Bevformer v2: Adapting modern image backbones to bird’s-eye-view recognition via perspective supervision. In *Proceedings of the IEEE/CVF Conference on Computer Vision and Pattern Recognition*. 17830–17839.
- [53] Tong Zhao, Peilin Guo, Junxiang He, and Yintao Wei. 2023. A hierarchical scheme of road unevenness perception with lidar for autonomous driving comfort. *IEEE Transactions on Intelligent Vehicles* 9, 1 (2023), 2439–2448.
- [54] Tong Zhao, Yichen Xie, Mingyu Ding, Lei Yang, Masayoshi Tomizuka, and Yintao Wei. 2024. A road surface reconstruction dataset for autonomous driving. *Scientific data* 11, 1 (2024), 459.
- [55] Tong Zhao, Lei Yang, Yichen Xie, Mingyu Ding, Masayoshi Tomizuka, and Yintao Wei. 2024. RoadBEV: Road Surface Reconstruction in Bird’s Eye View. *arXiv preprint arXiv:2404.06605* (2024).
- [56] Hongyu Zhou, Zheng Ge, Zeming Li, and Xiangyu Zhang. 2023. Matrixvt: Efficient multi-camera to bev transformation for 3d perception. In *Proceedings of the IEEE/CVF International Conference on Computer Vision*. 8548–8557.